

# Microscopic Insights into the Effect of the Initial Gas–Liquid Interface on Hydrate Formation by *In-Situ* Raman in the System of Coalbed Methane and Tetrahydrofuran

Jing Cai, Tao Lv, Xiao-Sen Li,\* Chun-Gang Xu, Nicolas von Solms, and Xiaodong Liang

Cite This: *ACS Omega* 2021, 6, 35467–35475

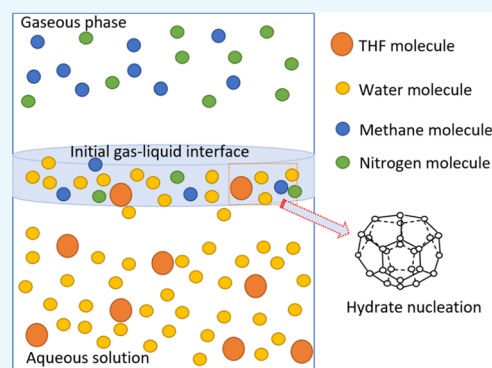
Read Online

ACCESS |

Metrics &amp; More

Article Recommendations

**ABSTRACT:** The serious issues of energy shortage and greenhouse gas emission have led to the development of coalbed methane (CBM) with new commercial ramifications. A hydrate-based gas separation technology is introduced to recover methane from CBM. However, the mechanism of hydrate nucleation needs to be clear for enhancing the hydrate formation rate and gas recovery efficiency. In this work, we studied, by means of *in-situ* Raman spectroscopy, the microscopic characterizations of hydrates forming in/around the initial gas–liquid interface in the case of CBM and tetrahydrofuran (THF). It is found that the hydrates accumulate as a film with horizontal crevices in the initial gas–liquid interface. These crevices prevent the hydrate film from hindering gas–liquid contact and limiting hydrate formation. Raman spectroscopy results illustrate that the initial gas–liquid interface shows a positive impact on water aggregation, and that the holding gas molecules stay stably with the water molecules. Nitrogen molecules engage into the cavities of THF hydrates along with methane molecules. For the interface and hydrate layer, water aggregation is evaluated by the Raman intensity ratio of hydrogen-bonded water (BW) and free water (FW) without any hydrogen bonds, abbreviated as  $I_{BW}/I_{FW}$ . A value of  $I_{BW}/I_{FW}$  higher than 0.85 can symbolize the occurrence of hydrate nucleation in the interface and help assess the hydrate formation.



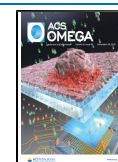
## 1. INTRODUCTION

Coalbed methane (CBM), also called coal mine methane (CMM), is a general term for all methane released in the process of coalification.<sup>1</sup> It is a mixture of mine methane and air emitted from coal mining to protect the underground coal mines from the risk of explosion and the unsafety possibility of an oxygen-poor atmosphere.<sup>1</sup> The methane composition in CBM generally ranges from 30 to 50 mol %, with a balance of oxygen and nitrogen.<sup>2</sup> For the benefits of energy production and greenhouse gas reduction, methane is to be captured and recovered from CBM.<sup>3,4</sup> This environment-friendly requirement has led to the development of CBM with a new commercial ramification.

Despite the conventional technologies of cryogenic separation,<sup>5</sup> pressure-swing adsorption,<sup>6</sup> and membrane,<sup>7,8</sup> hydrate-based gas separation technology is widely used to recover methane from CBM with various gas compositions.<sup>9</sup> The principle of hydrate-based methane recovery is based on the selective partition of the target component (methane) between the hydrate phase and gaseous phase.<sup>10</sup> For instance, the equilibrium pressure for methane hydrate, nitrogen hydrate, and methane–nitrogen binary hydrate in mixed gas with the methane content of 50.25 mol % is 5.02, 28.29, and 6.13 MPa, respectively, at around 279.15 K.<sup>11–13</sup> This shows that the

hydrate process could achieve a good gas selectivity for methane in comparison with nitrogen by controlling the hydrate formation conditions. In addition, methane can be effectively stored and easily transported in the form of methane hydrate based on its special gas storage capacity and stability conditions.<sup>14</sup> Generally, one cubic meter of methane hydrate can store ~164 cubic meters of methane gas at standard-state conditions when all cavities are engaged by methane molecules.<sup>15</sup> Moreover, methane hydrate could be stably transported under a mild stable condition of atmospheric pressure and 258.15 K.<sup>16</sup> Gudmundsson and Graff<sup>17</sup> considered that methane hydrate is an excellent form to transport methane for small-to-medium-size field discoveries, and its cost is lower relative to methane transport of liquefied natural gas and pipeline. These advantages of methane hydrate are highly suitable for coalbed methane reservoirs, which are generally located in remote areas and show complex character-

Received: September 6, 2021  
Accepted: December 1, 2021  
Published: December 14, 2021



istics.<sup>18</sup> Obviously, the hydrate process is not only an effective method to capture methane from CBM, but also a potential choice to transport CBM from the remote location. Therefore, researchers have been aspiring to find solutions for critical problems such as how to enhance the gas separation efficiency, gas consumption, and hydrate formation rate, and how to reduce the induction time and promote this technology in the industry.

For accelerating the formation rate and developing gas capacity, two aspects of investigations are generally carried out on additives and the gas–liquid contact area. The additives generally include thermodynamic promoters (cyclopentane (CP), quaternary ammonium salts, and tetrahydrofuran (THF)) and kinetic promoters (sodium dodecyl sulfate (SDS) and sodium dodecyl benzene sulfonate (SDBS)).<sup>10,19–26</sup> Thermodynamic promoters are widely introduced because they could moderate the hydrate formation conditions of pressure and temperature, and they also provide the bonus of enhancing the separation efficiency. For instance, in the hydrate formation system containing CP, the hydrate formation pressure could be reduced to 2.6 MPa at 283.4 K. The methane component could be achieved up to 47.2 and 72 mol % from 30 mol % in the feed gas by a single-stage and two-stage process, respectively.<sup>20</sup> Quaternary ammonium salts, like tetrabutylammonium bromide (TBAB) and tetrabutylammonium chloride (TBAC), as soluble inorganic promoters were widely adopted to accelerate the hydrate formation and/or enhance the separation efficiency. TBAB shows similar limitations on methane selectivity as CP; the methane content was only increased up to the range of 41–43 mol % from 30 mol % in the CBM feed gas.<sup>21,24</sup> By single-stage separation, the methane content was only increased to 67.86 from 46.25 mol %.<sup>28</sup> By the three-stage hydrate process, the methane content could be increased to 81.3 from 34.6 mol %.<sup>29</sup> However, the methane selectivity decreases with the increase of TBAB concentration. TBAC was reported to show a similar achievement on methane recovery as TBAB.<sup>25</sup> Besides, tetra-*n*-butylphosphonium bromide (TBPB) was also adopted to capture the methane from mine ventilation air with extremely low methane content, whereby the methane could be enriched by around 3.5-fold via the hydrate process.<sup>30</sup> Moreover, a high dose of quaternary ammonium salt needs to be added to form a massive hydrate for enhancing the cage occupancy of methane molecules and reducing the induction time of hydrate formation<sup>31</sup> because the cations of tetra-*n*-butylammonium (TBA<sup>+</sup>) or phosphonium (TBP<sup>+</sup>) involve in forming a part of the cage-lattice of the hydrate cavities.<sup>32</sup> THF as a famous hydrate promoter was firstly introduced to capture methane from CBM by Zhang et al.<sup>23</sup> The methane content could be increased in the range of 38.06–41.76 mol % from 26.00 mol % by adding a THF concentration of 1.0 mol %.<sup>23</sup> Zhao et al.<sup>26</sup> contrasted the effect of the thermodynamic promoter of THF and the kinetic promoter of SDS on methane recovery in a cyclic reactor. However, the methane component failed to be increased more by adding the kinetic promoter of SDS, because more nitrogen molecules are dissolved into solution and part of them are engaged into the hydrate cavities because of the decrease in surface tension.<sup>22</sup> The microscopic result testified that nitrogen molecules could engage into small cavities together with methane molecules.<sup>27</sup> In THF solution, the methane content could be increased up to 87.2 from 65.7 mol %, while in SDS solution, the methane content could only be increased to 69.7 mol %. Zhao et al. concluded that THF

showed a positive effect on methane recovery, but SDS only benefited on accelerating the hydrate formation. Further, the role of mixed additives, by adding the kinetic promoter into the THF solution, in improving both the hydrate formation and separation efficiency was investigated. For instance, by adding 500 ppm SDS, the methane content could be increased up to 69.93 from 50 mol %.<sup>10</sup> By adding the amino acid of L-tryptophan in THF solution,<sup>33</sup> although the hydrate formation rate could be increased to 130%, the selectivity of methane from CBM was still weak. The methane content only increased up to 56.8 from 30 mol % in the feed gas. Therefore, it was speculated that THF may show some special capture ability for methane molecules.

From the intrinsic point of view, the addition of thermodynamic and kinetic promoters is related to mass transfer among the gaseous phase, liquid phase, and hydrate phase. Adding thermodynamic promoters is of benefit for enhancing the driving force of mass transfer, which improves the transfer of compounds from gaseous phase and liquid phase towards the hydrate phase. By adding kinetic promoters, the surface intension can be reduced significantly, which could trigger the diffusion of massive compounds from gaseous phase towards the liquid phase, further improving the mass transfer towards the hydrate phase. In other words, the driving force of mass transfer and the gas–liquid contact velocity can be strengthened by reducing the mass transfer resistance. Apart from the addition of hydrate promoters, the gas–liquid contact velocity could also be improved by changing the gas–liquid contact patterns with different hydrate crystallizers. Zhong et al.<sup>34,35</sup> reported that a fixed bed of silica sand could increase the hydrate formation rate and enhance the methane recovery. They produced a water-in-oil (W/O) emulsion to improve methane separation by adding mineral oil, sorbitan monooleate (Span 80), and cyclopentane.<sup>36</sup> In addition, a superabsorbent polymer and graphite nanofluid were adopted to increase the methane content from CBM.<sup>37,38</sup> The spray reactor could enlarge the gas–liquid contact area and showed a positive impact on enhancing the hydrate formation rate and gas storage capacity.<sup>39,40</sup> Besides, a new gas–liquid contact pattern was used in the scale-up bubbling reactor, which was also introduced to capture methane from CBM.<sup>41</sup> The experimental results proved that the hydrate-based gas separation technology could be easily carried out on a pilot scale. At the same time, they also indicated that the hydrates initially formed at the boundary of bubbles, gradually grew up with the shell sticking around the bubbles, and finally accumulated in the gas–liquid interface. As mentioned above, the gas–liquid interface is involved in all hydrate formation processes in various formation systems and formation reactors. It is critical to clear the mass transfer process in the initial gas–liquid interface and hydrate formation interface for understanding the mechanism of hydrate formation and obtaining various hydrates in a controlled manner.

In this work, we focused on the measurement of the initial gas–liquid interface and the hydrate layer by using *in-situ* Raman spectroscopy. Especially, the initial gas–liquid interface was generated by water, the most popular soluble hydrate promoter of THF,<sup>10,19,41</sup> and CBM simulation gas (methane/nitrogen gas mixture). All experiments were carried out in a static system with a constant volume. The compounds in/around the initial gas–liquid interface and the hydrate layer were monitored in real time using *in-situ* Raman spectroscopy in the process of hydrate formation. Besides, the macroscopic

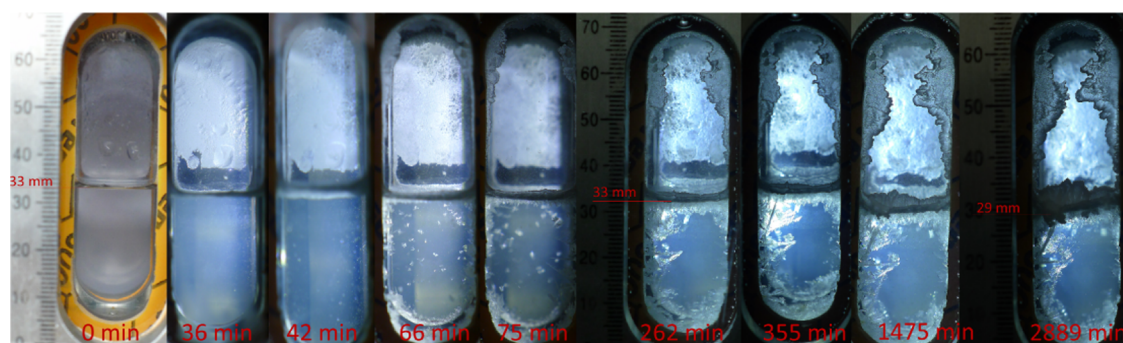


**Figure 1.** Morphology of hydrate formation at different times in the process of hydrate formation.

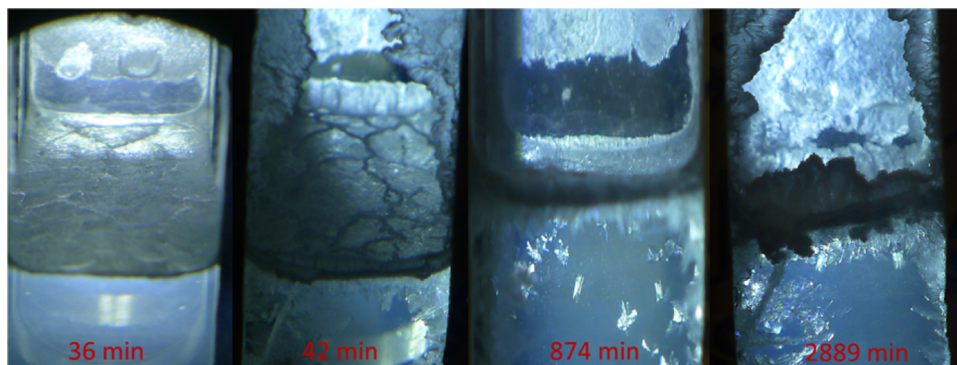


**Figure 2.** Morphological details for the hydrate formation interface at the position of the initial gas–liquid interface.

morphology of hydrate formation was photographed by a camera (Nikon7100).

## 2. RESULTS AND DISCUSSION

In the process of hydrate formation, the hydrates generally occur at the initial gas–liquid interface and gradually accumulate as a hydrate film at the interface. This film was reported as the negative factor,<sup>42</sup> which hindered the mass transfer from the gaseous phase towards liquid phase and hydrate phase, and, consequently, limited the hydrate formation rate and separation efficiency. However, a different macroscopic morphology of the hydrate film was observed in this work. To clear its mass transfer, the effect of the initial gas–liquid interface on hydrate formation was investigated by using *in-situ* Raman spectroscopy from the microscopic point of view. All experiments were carried out with 40 mol % methane/nitrogen gas mixture and 1.0 mol % THF solution at the conditions of 273.15 K and 3.50 MPa.

### 2.1. Macroscopic Morphology of Hydrate Formation.

Figure 1 shows the macroscopic morphology of hydrate formation with the whole window view at different times. Before hydrate formation, it can be observed that the initial gas–liquid interface obviously occurs at the position around 33 mm, with a limited curving surface and a clear boundary between the gaseous phase and the bulk solution. In addition, due to the hydrophobicity of the quartz glass and the stainless-steel walls, the initial gas–liquid interface shows a pseudo-visual thickness. Its value is around 0.5 mm in the vertical direction, which is measured from the side ruler on the crystallizer. In theory, the thickness of such an initial gas–liquid interface could be extremely limited. However, in reality, the initial gas–liquid interface shows in the form of a thin layer. Here, we suppose it as the thin layer with mass flux,

consisting of the top and bottom mass transfer interfaces with regenerative characteristics. In the process of hydrate formation, they could convert to initial gas hydrate formation interfaces. As shown in Figure 1, the hydrate film always locates at the same position of around 33 m before 1475 min.

From Figure 1, it can be found that the hydrate film keeps at around 33 m from 36 min to 355 min, while it moves downward at the position of around 29 mm since 1475 min. Moreover, the macroscopic morphology of the hydrate film changes with hydrate formation. At the bottom of the hydrate film, it can be found that its fluff boundary gradually moves towards into the bulk solution after 36 min and sticks to the hydrate crystals with various morphologies. At 42 min, tiny hydrate particles grow from the bottom of the hydrate film. At 66 min, the needle hydrates gradually appear, and they grow towards the bulk solution at 75 min, showing a bigger size. From 262 to 355 min, the hydrate film obviously thickens and grows into the bulk solution along the crystallizer walls and window. Since 1475 min, the hydrate film shifts downwards around 29 mm. Moreover, the hydrate film also shows a growing trend upwards to the gaseous phase from 42 to 355 min, and the upper hydrate film grows shapely along the crystallizer walls and window in the same way as the one at the bottom of the hydrate film. All these macroscopic phenomena illustrate that the initial gas–liquid interface is reasonable to be treated as a thin layer with mass flux, and it can convert to the hydrate formation interfaces. With the substances updating at the top and bottom of this initial thin layer, the hydrates firstly form at the bottom of the initial gas–liquid interface and gradually accumulate as a hydrate film, as described above.

From Figure 2, the morphological details for the top and bottom hydrate film can be observed. Obvious crevices can be found in the hydrate film at 36 min, and the width of the



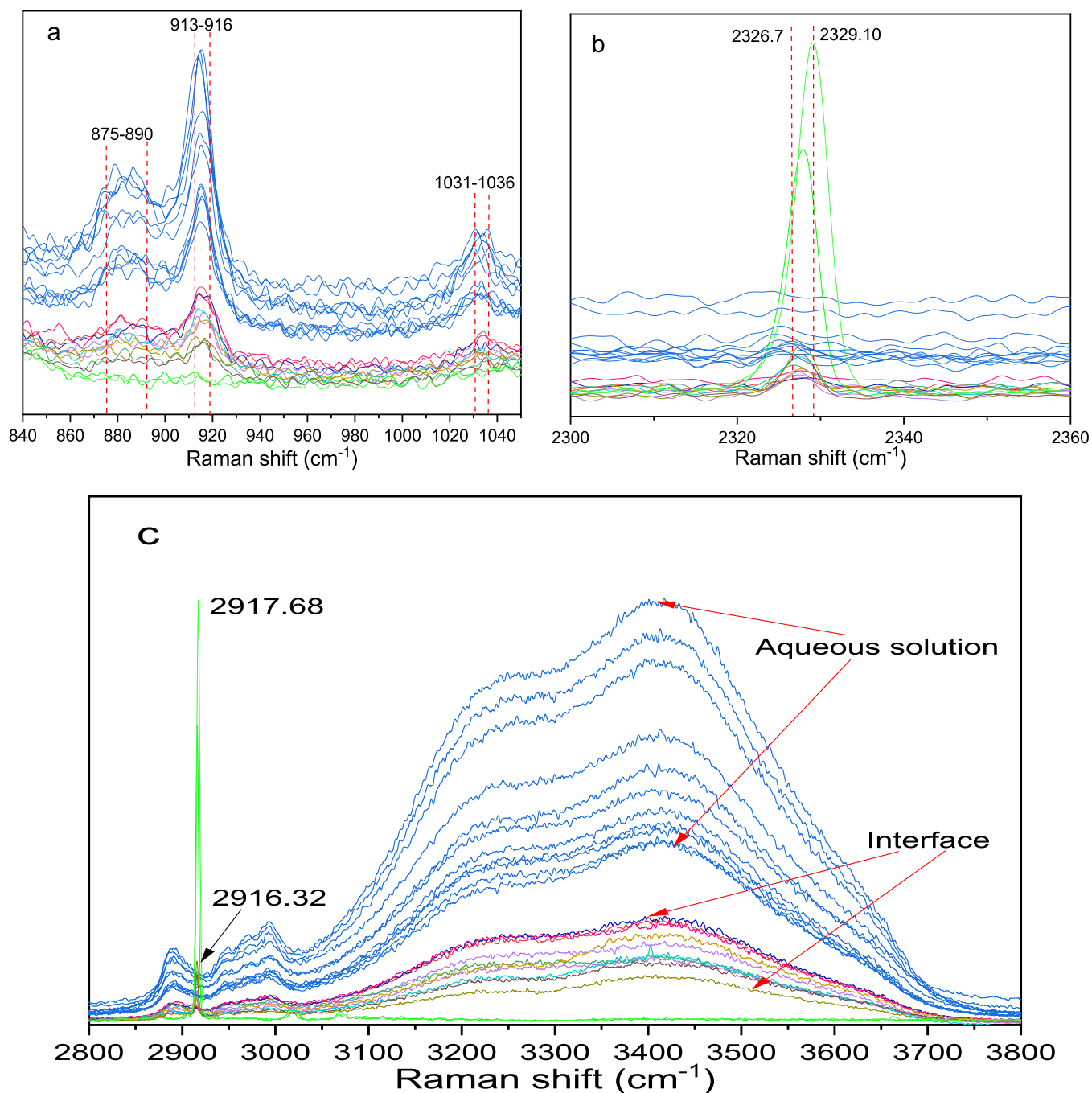


**Figure 3.** Raman spectra for compounds before the hydrate formation at 3.50 MPa and room temperature. The gaseous phase is shown by the green lines; the bulk phase (blue lines) close to the initial gas–liquid interface (multicolored lines) detailing the various Raman shifts of 840–960  $\text{cm}^{-1}$  (a), 2300–2360  $\text{cm}^{-1}$  (b), and 2800–3800  $\text{cm}^{-1}$  (c) is shown.

crevices increase at 42 min; accordingly, the hydrate film is cracked significantly as a floating film. Similar cracks were reported in the perpendicular direction to the interface.<sup>42</sup> Subsequently, this kind of hydrate film accumulating in the initial gas–liquid interface gradually grows towards the gaseous phase and bulk solution along the crystallizer walls and window after 262 min, as shown in Figure 1. The same growth trend can be found in detail at 874 and 2889 min in Figure 2. In the upper hydrate film, the hydrate grows towards the gaseous phase in the form of a gel with a clear column. A similar hollow crater-like formation was reported in the THF solution by Veluswamy et al., and the driving force was supposed to be

continuous gas–liquid contact through the thin channels in the hydrate film.<sup>43</sup> From the bottom of the hydrate film, the hydrate crystallizes towards the bulk solution in the form of a whisker with clear planes, where the driving force was supposed to be the subcooling and the concentration of the dissolved gas and promoters.<sup>44</sup> In this work, all these phenomena indicate that there are various mass transfer patterns in the process of hydrate formation. However, the hydrate film accumulating in the gas–liquid interface could not be simply concluded as a negative factor that hinders the mass transfer from gaseous phase towards liquid phase and hydrate phase, further reducing the hydrate formation rate and limiting

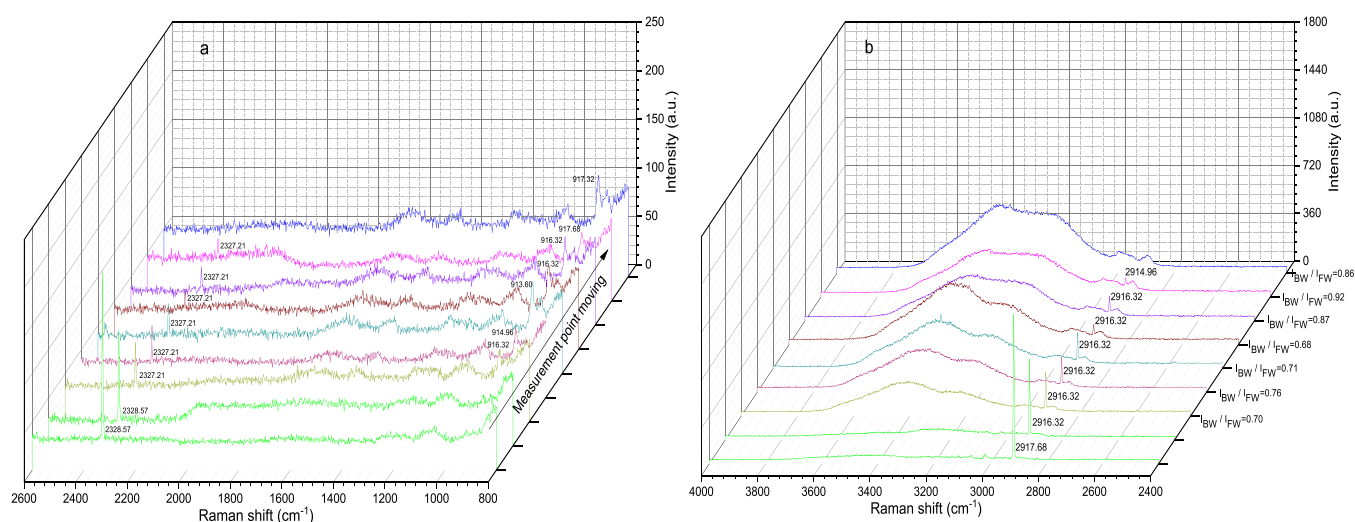


**Figure 4.** Raman spectra for compounds in the initial gas–liquid interface. The gaseous phase is shown by the green lines; the bulk phase (blue lines) close to the initial gas–liquid interface (multicolored lines) detailing the various Raman shifts of 800–2600  $\text{cm}^{-1}$  (a) and 2400–4000  $\text{cm}^{-1}$  (b) is shown.

the gas separation efficiency, as reported in the literature.<sup>45,46</sup> As shown in Figure 2, the hydrate film with the horizontal crevices is firstly observed, and such a hydrate film does not prevent the gas–liquid contact and further limit the hydrate formation. In addition, in Figure 1, visible whiskery hydrate particles floating in the solution and flake hydrates sticking to the windows can also be found in the bulk solution and in gaseous phase, respectively. These phenomena also prove that the mass transfer is complicated in the hydrate formation system with a single gas–liquid interface. It is difficult to understand the mechanism of hydrate formation only from the macroscopic point of view. Advanced analytical techniques need to be adopted to understand the distinct mass transfer from the microscopic point of view by combining with morphological observations. Therefore, *in-situ* Raman spectroscopy was employed to characterize the initial gas–liquid interface and the hydrate film mentioned above.

**2.2. Raman Spectra for Compounds before and during the Process of Hydrate Formation.** Figure 3 shows the Raman spectra for the compounds before hydrate formation under the conditions of 3.50 MPa and room temperature. Especially, all compounds in gaseous phase, interface, and bulk solution were measured. For THF molecules, as shown in Figure 3a, the two groups of Raman peaks at 875–890 and 913–916  $\text{cm}^{-1}$  correspond to the ring breathing (C–C–C–C stretching) mode of THF. This C–C–C–C stretching mode could be degenerated into two splitting Raman peaks due to the intermolecular forces with water molecules in aqueous solution.<sup>47,48</sup> From the blue lines, these two groups of Raman peaks can be distinguished clearly in the bulk solution, but from the green line, there are no related Raman peaks of THF molecules that can be found in gaseous phase. From the multicolored lines, the group of Raman peaks at 913–916  $\text{cm}^{-1}$  can still be observed in the interface, while no obvious Raman peaks at around 875–890  $\text{cm}^{-1}$  can be identified. This kind of Raman spectra is similar to those of THF molecules engaged into the hydrate cavities.<sup>49,50</sup> It illustrates that the force field around the THF molecules in the initial gas–liquid interface is changed and the vibrational motions of THF molecules are restricted because of the initial gas–liquid interface. The shape and intensity of the Raman

peaks of THF molecules in the initial gas–liquid interface are similar to those of the THF molecules engaged into the hydrate cavities.<sup>51,52</sup> We considered that the initial gas–liquid interface could target the water molecules around the THF molecules to arrange like the hydrate cavities, further improving the hydrate nucleates in the initial gas–liquid interface at the suitable temperature. In addition, as shown in Figure 3c, the Raman peaks at 1031–1036  $\text{cm}^{-1}$  correspond to the weak mode of the C–O–C symmetric stretching of the THF molecules.<sup>47</sup> The Raman peaks between  $\sim 2800$  and  $\sim 3000$   $\text{cm}^{-1}$  correspond to the C–H stretching vibration of the THF molecules. The slight differences between the groups of Raman peaks obtained in the bulk solution and those in the interface further illustrate that the initial gas–liquid interface may be having a positive impact on adjusting the planar steric hindrance of the THF molecules.

Figure 4 shows the Raman peaks for the compounds in the initial gas–liquid interface from its top and bottom. In section 2.1, the initial gas–liquid interface could be treated as a thin layer with mass flux, consisting of the top and bottom mass transfer interfaces with regenerative characteristics, based on the morphology of hydrate formation. Microscopic analysis on this thin layer with top and bottom mass transfer interfaces was done in detail by *in-situ* Raman. For nitrogen molecules, from Figures 3b and 4a, the Raman peaks corresponding to the N–N triple bond vibration of nitrogen molecules can be observed in both gaseous phase and the interface. Moreover, the Raman peaks of the nitrogen molecules red-shift to around 2327  $\text{cm}^{-1}$  in the interface compared with those at around 2329  $\text{cm}^{-1}$  in the gaseous phase. However, no Raman peaks for nitrogen molecules can be found in the bulk solution, which is similar to the Raman peaks for nitrogen molecules in the bulk solution with hydrate formation. As shown in Figure 5, no Raman peak for nitrogen molecules is detected in the bulk solution even with the existence of massive hydrates. This proves that it is difficult for nitrogen molecules to stay stably with water molecules or dissolve in the bulk solution. However, the initial gas–liquid interface can affect the aggregation of nitrogen molecules and help them stay in the interface. For methane molecules, from Figures 3b and 4b, the Raman peaks of methane molecules red-shift from  $\sim 2917$   $\text{cm}^{-1}$  in the gaseous

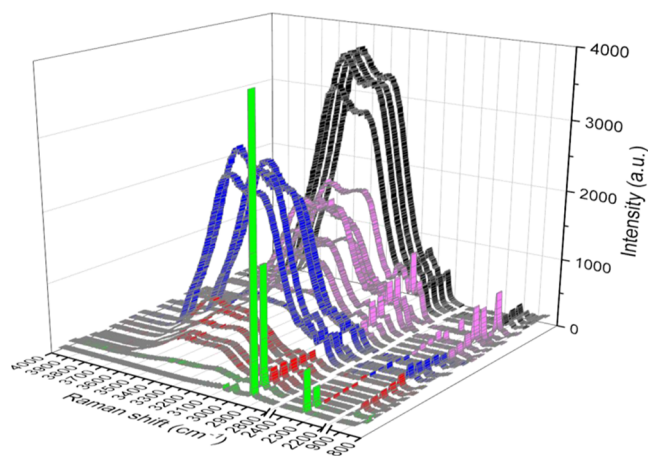


**Figure 5.** Raman spectra for compounds in the gaseous phase (green), hydrate layers (red, blue and pink), and aqueous solution (black) at 2889 min under the conditions of 273.15 K and 3.50 MPa.

phase to  $\sim 2914\text{ cm}^{-1}$  in the interface. This Raman shift is similar to the Raman shift of nitrogen molecules in the interface, which also evidences that the aggregation of methane molecules is influenced by the interface. From Figure 4, it can be found that the intensity of Raman peaks for methane molecules and nitrogen molecules gradually decreases with the measurement point moving from the top to the bottom of the initial gas–liquid interface. Meanwhile, the intensity of Raman peaks for THF molecules at  $\sim 913\text{--}916\text{ cm}^{-1}$  gradually increases. All these phenomena prove that the compounds are significantly affected by the initial gas–liquid interface. Moreover, from the top to the bottom, the distribution of compounds shows a weak decreasing gradient of Raman intensity for methane and nitrogen molecules and a weak increasing concentration gradient for THF molecules.

For water molecules, a Raman intensity ratio of hydrogen-bonded water (BW) and free water (FW) without any hydrogen bonds is introduced to evaluate the water aggregation in the hydrate system, which is abbreviated as  $I_{\text{BW}}/I_{\text{FW}}$  in this work. The lower value of  $I_{\text{BW}}/I_{\text{FW}}$  illustrates higher water aggregation.<sup>49</sup> As shown in Figures 3c and 4b, the value of  $I_{\text{BW}}/I_{\text{FW}}$  in the initial gas–liquid interface shows a slight increasing trend from the top to the bottom of the interface, where the value increases from  $\sim 0.70$  to  $0.92$ , showing the inhomogeneous characteristics. Moreover, the value at the bottom of interface is higher than that of the bulk solution with  $0.86$ . This phenomenon is consistent with the conclusion reported in the literature<sup>53,54</sup> that the hydrate nucleation prefers to occur at the interface close to the aqueous solution. That is, the initial gas–liquid interface affects the water aggregation, benefiting the generation of positive structures to form the hydrates. As mentioned above, the initial gas–liquid interface also influences the ring breathing mode of THF molecules and helps nitrogen and methane molecules to stay stably with the water molecules. In sum, this proves that the initial gas–liquid interface could have a positive impact on the rearrangement or aggregation of molecules, and the initial gas–liquid interface could be hypothesized as a thin inhomogeneous layer with mass flux. Moreover, the hydrate nucleation near the bottom of the gas–liquid interface precedes that at the top of the interface.

After measuring the initial gas–liquid interface, the hydrate formation layer was also measured using *in-situ* Raman

spectroscopy. As shown in Figure 5, the Raman spectra for compounds in gaseous phase, the hydrate layer, and aqueous solution at 2889 min are detailed. The morphology of this hydrate layer can be found in Figures 2 and 3. For the THF molecules, clear Raman peaks can be found at  $\sim 919\text{ cm}^{-1}$  in the hydrate layer (shown by the red, blue, and pink parts), which represent THF molecules encaging into the hydrate cavities.<sup>47,48,55–57</sup> For the gas molecules, it can be found that methane molecules can be detected in the gaseous phase, hydrate layer, and bulk solution, while nitrogen molecules can only be detected in the gaseous phase and hydrate layer. This phenomenon proves that nitrogen molecules can encage into the THF hydrate cavities together with methane molecules. For the water molecules, their irregular distribution can be observed in the hydrate layer, which is consistent with the results in the literature.<sup>49,53</sup> Based on these Raman peaks of water molecules, the Raman spectra for the hydrate layer can be divided into three different parts, shown by the red, blue, and pink parts. The red and pink parts illustrate that the strict water aggregation with hydrate cavities mainly occurs at the boundary of the hydrate layer, located at the top and bottom of the hydrate layer, respectively. The blue part illustrates that water molecules without strict cavities are detected in the body hydrate layer, and some Raman peaks for methane and nitrogen molecules are detected there as well. Therefore, we speculate that two different hydrate formation interfaces are involved in the process of hydrate formation, which are converted to form the top and bottom interfaces of the initial gas–liquid interface. Moreover, water molecules could be rearranged in the hydrate layer between these two hydrate formation interfaces.

To observe the effect of the initial gas–liquid interface on water aggregation, the values of  $I_{\text{BW}}/I_{\text{FW}}$  in the hydrate formation system before and during the process of hydrate formation are compared in Figure 6. The measurement point

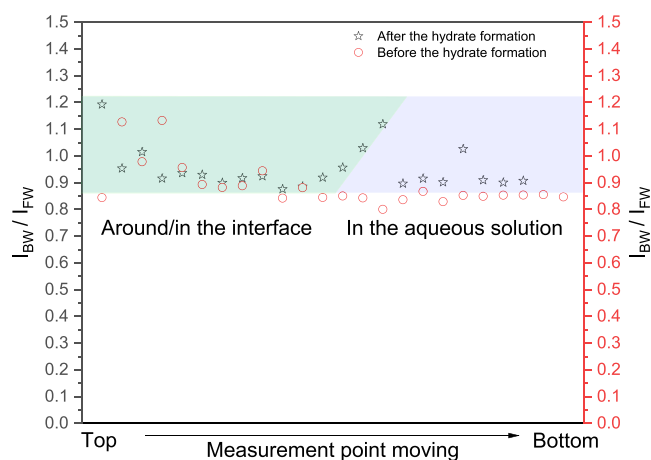


**Figure 6.** Comparison of  $I_{\text{BW}}/I_{\text{FW}}$  in the system before and during the process of hydrate formation.

moved from the gaseous phase (light blue zone) towards the bulk solution (light gray zone) close to the initial gas–liquid interface. These measurement points covered the whole initial gas–liquid interface. From Figure 6, it can be found that the values of  $I_{\text{BW}}/I_{\text{FW}}$  are always higher than  $0.85$  after hydrate formation, which indicates water aggregation in the form of hydrogen bonding. However, before hydrate formation, most values of  $I_{\text{BW}}/I_{\text{FW}}$  obtained in/around the initial gas–liquid



interface are higher than 0.85, while the values obtained in the aqueous solution are lower than 0.85 (between 0.75 and 0.85), as detailed in Figure 4b. These values further prove that the initial gas–liquid interface benefits by improving water aggregation in the form of cavities, which helps the gas molecules to stay stably with the water molecules as well. Similar values of  $I_{\text{BW}}/I_{\text{FW}}$  (higher than 0.85) are found in the initial gas–liquid interface and the hydrate layer, which correlates to the water aggregation benefiting the hydrate formation. Therefore, it is deemed that the intensity ratio of  $I_{\text{BW}}/I_{\text{FW}}$  with the value of 0.85 can be adopted to evaluate the hydrate nucleation.

### 3. CONCLUSIONS

In this work, a hydrate-based methane recovery technology was investigated in the system of coalbed methane and THF solution at 273.15 K and 3.50 MPa. The effect of the initial gas–liquid interface on hydrate nucleation was studied by using *in-situ* Raman spectroscopy, and the morphology was recorded by a camera in the process of hydrate formation. Based on the Raman spectra for compounds in/around the initial gas–liquid interface, it can be found that the initial gas–liquid interface shows a positive impact on water aggregation, and that the gas molecules stay stably with the water molecules. The initial gas–liquid interface can be hypothesized as an inhomogeneous thin layer with mass flux, which can convert to the hydrate film in the process of hydrate formation. From the morphology, it was observed that obvious crevices in the hydrate film can supply continuous mass transfer channels for hydrate formation instead of hindering the gas–liquid contact. Raman spectroscopic results also illustrate that nitrogen molecules can engage into the THF hydrate together with methane molecules. Water aggregation evaluated by the Raman intensity ratio of hydrogen-bonded water (BW) and free water (FW) without any hydrogen bonds, abbreviated as  $I_{\text{BW}}/I_{\text{FW}}$ , shows that the water molecules are transferring into and out of the cavities of THF hydrates in the hydrate layer, and its value (higher than 0.85) can be employed to evaluate hydrate nucleation.

### 4. EXPERIMENTAL SECTION

Methane/nitrogen gas mixture with a methane composition of 40 mol % was used to simulate coalbed methane (CBM), which was supplied by Foshan Huate Special Gas Co., Ltd., China. Tetrahydrofuran (THF) with a purity of 99.9% was purchased from Chengdu Best Reagent Co., Ltd., China. Deionized water with the resistivity of 18.25 M $\Omega$ -cm at room temperature was produced by an ultrapure water system supplied by Nanjing Ultrapure Water Technology Co., Ltd., China. The details of the apparatus can be found in our previous work.<sup>49,53</sup>


The main experimental procedure is as follows: First, 1.0 mol % THF solution with the volume of 45 mL was added into the crystallizer. Then, the crystallizer was sealed and the methane/nitrogen gas mixture was injected to wash the crystallizer three times in order to be air-free. Later, the crystallizer was pressurized up to the desired pressure of 3.50 MPa at room temperature. The crystallizer was kept to reach the dissolution equilibrium of the gas mixture. Subsequently, the compounds in/around the initial gas–liquid interface, in the gaseous phase, and in the aqueous phase were comprehensively characterized using the *in-situ* Raman

spectrometer. After measurement, the crystallizer was covered with stainless-steel jackets to cool the crystallizer for hydrate formation. These jackets were filled with glycol solution and connected to a refrigerator. While the crystallizer temperature was stable at around 273.15 K, the initial gas–liquid interface was measured in real time using the *in-situ* Raman spectrometer for monitoring the occurrence of hydrates. With the hydrate accumulation in the interface, the hydrate layer was characterized as well. All experiments were carried out under the static condition without stirring and with continuous gas supply.

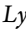
In this work, all *in-situ* Raman measurements were performed using a LabRAM HR800 confocal microscope (Horiba Jobin Yvon). The hydrates in the crystallizer were characterized using a green laser with the wavelength of 532 nm, with an air-cooled argon ion laser as the excitation source. The output power of this green laser was 100 mW. The scattered light was dispersed through a single monochromator system with a groove density of 600 grooves/mm, which was connected to a multichannel charge-coupled device (CCD) detector. A long-working-distance lens, including an objective lens (1 time magnification), a UV corner lens, and a chamfer tube, was employed to introduce the scattered light to nondestructively characterize the hydrate samples in the crystallizers. The spot diameter was around 2  $\mu\text{m}$ , and the Raman signal was collected from the spot confocal geometry. The hydrate samples could be characterized with high sensitivity and high spatial resolution, and the Raman measurements were repeatable with a precision of  $\pm 0.02 \text{ cm}^{-1}$ . The Raman spectrum was obtained by automatic scanning every 10 s.

### AUTHOR INFORMATION

#### Corresponding Author

Xiao-Sen Li – Guangzhou Institute of Energy Conversion and Key Laboratory of Gas Hydrate, Chinese Academy of Sciences, Guangzhou 510640, P. R. China; Guangdong Provincial Key Laboratory of New and Renewable Energy Research and Development, Guangzhou 510640, P. R. China;  [orcid.org/0000-0001-8608-0950](https://orcid.org/0000-0001-8608-0950); Email: [lixs@ms.giec.ac.cn](mailto:lixs@ms.giec.ac.cn)

#### Authors

Jing Cai – Guangzhou Institute of Energy Conversion and Key Laboratory of Gas Hydrate, Chinese Academy of Sciences, Guangzhou 510640, P. R. China; Guangdong Provincial Key Laboratory of New and Renewable Energy Research and Development, Guangzhou 510640, P. R. China; Center for Energy Resources Engineering, Department of Chemical and Biochemical Engineering, Technical University of Denmark, Lyngby 2800, Denmark;  [orcid.org/0000-0002-6311-0210](https://orcid.org/0000-0002-6311-0210)

Tao Lv – College of Petroleum Engineering, Xi'an Shiyou University, Xi'an 710065, P. R. China

Chun-Gang Xu – Guangzhou Institute of Energy Conversion and Key Laboratory of Gas Hydrate, Chinese Academy of Sciences, Guangzhou 510640, P. R. China; Guangdong Provincial Key Laboratory of New and Renewable Energy Research and Development, Guangzhou 510640, P. R. China

Nicolas von Solms – Center for Energy Resources Engineering, Department of Chemical and Biochemical Engineering, Technical University of Denmark, Lyngby 2800, Denmark

Xiaodong Liang – Center for Energy Resources Engineering,  
Department of Chemical and Biochemical Engineering,  
Technical University of Denmark, Lyngby 2800, Denmark;  
orcid.org/0000-0002-2007-546X

Complete contact information is available at:  
<https://pubs.acs.org/10.1021/acsomega.1c04907>

## Notes

The authors declare no competing financial interest.

## ACKNOWLEDGMENTS

This work was supported by the Key Program of the National Natural Science Foundation of China (51736009, 51676190), Guangdong Special Support Program-Local Innovation and Entrepreneurship Team Project (2019BT02L278), Special Project for Marine Economy Development of Guangdong Province (GDME-2018D002, GDME-2020D044), Youth Innovation Promotion Association CAS (2018382), Science and Technology Apparatus Development Program of the Chinese Academy of Sciences (YJKYYQ20200061), Fundamental Research & Applied Fundamental Research Major Project of Guangdong Province (2019B030302004, 2020B0301030003), Guangdong International Talent Training Program-Postdoctoral Project (2019001), and Key Laboratory Fund of Gas Hydrate (E029020201), all of which are gratefully acknowledged.

## REFERENCES

- Lea, J. F.; Nickens, H. V.; Wells, M. R. Coal Bed Methane. In *Gas Well Deliquification*, 2nd edition; Gulf Professional Publishing, 2008; 405–422. <https://doi.org/10.1016/b978-075068280-0.50015-9>.
- Pagan, R.; Price, N.; Prasad, P. Managing the Environmental Impact of the Dairy Industry: The Business Case for Sustainability. *Improv. Saf. Qual. Milk: Improv. Qual. Milk Prod.* **2010**, 252–280.
- Yang, M. Climate Change and Energy Policies, Coal and Coalmine Methane in China. *Energy Policy* **2009**, 37, 2858–2869.
- Karacan, C. Ö.; Ruiz, F. A.; Cotè, M.; Phipps, S. Coal Mine Methane: A Review of Capture and Utilization Practices with Benefits to Mining Safety and to Greenhouse Gas Reduction. *Int. J. Coal Geol.* **2011**, 86, 121–156.
- Xiao, L.; Chen, J. Experimental Study on Distillation Column Parameters for Liquefaction Device of Low Concentration Coalbed Methane. *Processes* **2021**, 9, No. 606.
- Lu, B.; Shen, Y.; Tang, Z.; Zhang, D.; Chen, G. Vacuum Pressure Swing Adsorption Process for Coalbed Methane Enrichment. *Chin. J. Chem. Eng.* **2021**, 32, 264–280.
- Kim, S.; Ko, D.; Row, S. W.; Kim, J. Techno-Economic Evaluation of Hybrid Systems of Pressure Swing Adsorption and Membrane Processes for Coalbed Methane Separation. *Chem. Eng. Res. Des.* **2016**, 115, 230–240.
- Zhang, N.; Pan, Z.; Zhang, L.; Zhang, Z. Decarburization Characteristics of Coalbed Methane by Membrane Separation Technology. *Fuel* **2019**, 242, 470–478.
- Li, X. Y.; Ge, B.; Bin, Yan, J.; Lu, Y. Y.; Zhong, D. L.; Englezos, P.; Zhang, B. Y. Review on Hydrate-Based CH<sub>4</sub> Separation from Low-Concentration Coalbed Methane in China. *Energy Fuels* **2021**, 35, 8494–8509.
- Li, X. Sen.; Cai, J.; Chen, Z. Y.; Xu, C. G. Hydrate-Based Methane Separation from the Drainage Coal-Bed Methane with Tetrahydrofuran Solution in the Presence of Sodium Dodecyl Sulfate. *Energy Fuels* **2012**, 26, 1144–1151.
- van Cleeff, A.; Diepen, G. A. M. Gas Hydrates of Nitrogen and Oxygen. II. *Recl. des Trav. Chim. des Pays-Bas* **1965**, 84, 1085.
- Jhaveri, J.; Robinson, D. B. Hydrates in the Methane-nitrogen System. *Can. J. Chem. Eng.* **1965**, 43, 75–78.
- Adisasmito, S.; Frank, R. J.; Sloan, E. D. Hydrates of Carbon Dioxide and Methane Mixtures. *J. Chem. Eng. Data* **1991**, 36, 68–71.
- Mokhatab, S.; Poe, W. A.; Mak, J. Y. *Handbook of Natural Gas Transmission and Processing: Principles and Practices*, 3rd ed.; 2015. <https://doi.org/10.1016/C2013-0-15625-5>.
- Makogon, Y. F. Natural Gas Hydrates - A Promising Source of Energy. *J. Nat. Gas Sci. Eng.* **2010**, 2, 49–59.
- Gudmundsson, J. S.; Parlaktuna, M.; Khokhar, A. A. Storing Natural Gas as Frozen Hydrate. *SPE Prod. Facil.* **1994**, 9, 69–73.
- Gudmundsson, J. S.; Graff, O. F.; Kvaerner, A. In *Hydrate Non-Pipeline Technology for La Technologie Du Transport Hors Pipe De Gas Naturel Sous Forme D' Hydrates*, 22nd World Gas Conference, 2003.
- Altowilib, A.; Alsayhathi, A.; Alhamood, H.; Alafnan, S.; Alarif, S. Reserves Estimation for Coalbed Methane Reservoirs: A Review. *Sustainability* **2020**, 12, No. 10621.
- Cai, J.; Xu, C. G.; Chen, Z. Y.; Li, X. Sen. Recovery of Methane from Coal-Bed Methane Gas Mixture via Hydrate-Based Methane Separation Method by Adding Anionic Surfactants. *Energy Sources, Part A* **2018**, 40, 1019–1026.
- Zhong, D. L.; Daraboina, N.; Englezos, P. Recovery of CH<sub>4</sub> from Coal Mine Model Gas Mixture (CH<sub>4</sub>/N<sub>2</sub>) by Hydrate Crystallization in the Presence of Cyclopentane. *Fuel* **2013**, 106, 425–430.
- Zhong, D.; Englezos, P. Methane Separation from Coal Mine Methane Gas by Tetra-n-Butyl Ammonium Bromide Semiclathrate Hydrate Formation. *Energy Fuels* **2012**, 26, 2098–2106.
- Zhong, D. L.; Ding, K.; Yan, J.; Yang, C.; Sun, D. J. Influence of Cyclopentane and SDS on Methane Separation from Coal Mine Gas by Hydrate Crystallization. *Energy Fuels* **2013**, 27, 7252–7258.
- Zhang, B.; Wu, Q. Thermodynamic Promotion of Tetrahydrofuran on Methane Separation from Low-Concentration Coal Mine Methane Based on Hydrate. *Energy Fuels* **2010**, 24, 2530–2535.
- Zhong, D. L.; Ye, Y.; Yang, C.; Bian, Y.; Ding, K. Experimental Investigation of Methane Separation from Low-Concentration Coal Mine Gas (CH<sub>4</sub>/N<sub>2</sub>/O<sub>2</sub>) by Tetra-n-Butyl Ammonium Bromide Semiclathrate Hydrate Crystallization. *Ind. Eng. Chem. Res.* **2012**, 51, 14806–14813.
- Zhong, D. L.; Wang, W. C.; Zou, Z. L.; Lu, Y. Y.; Yan, J.; Ding, K. Investigation on Methane Recovery from Low-Concentration Coal Mine Gas by Tetra-n-Butyl Ammonium Chloride Semiclathrate Hydrate Formation. *Appl. Energy* **2018**, 227, 686–693.
- Zhao, J.; Zhao, Y.; Liang, W. Hydrate-Based Gas Separation for Methane Recovery from Coal Mine Gas Using Tetrahydrofuran. *Energy Technol.* **2016**, 4, 864–869.
- Lee, J.; Jin, Y. K.; Seo, Y. Characterization of Cyclopentane Clathrates with Gaseous Guests for Gas Storage and Separation. *Chem. Eng. J.* **2018**, 338, 572–578.
- Sun, Q.; Guo, X.; Liu, A.; Liu, B.; Huo, Y.; Chen, G. Experimental Study on the Separation of CH<sub>4</sub> and N<sub>2</sub> via Hydrate Formation in TBAB Solution. *Ind. Eng. Chem. Res.* **2011**, 50, 2284–2288.
- Wang, Y.; Deng, Y.; Guo, X.; Sun, Q.; Liu, A.; Zhang, G.; Yue, G.; Yang, L. Experimental and Modeling Investigation on Separation of Methane from Coal Seam Gas (CSG) Using Hydrate Formation. *Energy* **2018**, 150, 377–395.
- Du, J.; Li, H.; Wang, L. Phase Equilibria and Methane Enrichment of Clathrate Hydrates of Mine Ventilation Air + Tetrabutylphosphonium Bromide. *Ind. Eng. Chem. Res.* **2014**, 53, 8182–8187.
- Chanakro, W.; Jaikwang, C.; Inkong, K.; Kulprathipanja, S.; Rangsunvigit, P. Comparative Study of Tetra-N-Butyl Ammonium Bromide and Cyclopentane on the Methane Hydrate Formation and Dissociation. *Energies* **2020**, 13, No. 6518.
- Jeffrey, G. A. Hydrate Inclusion Compounds. *J. Inclusion Phenom.* **1984**, 1, 211–222.
- Zhang, Q.; Zheng, J.; Zhang, B.; Linga, P. Coal Mine Gas Separation of Methane via Clathrate Hydrate Process Aided by Tetrahydrofuran and Amino Acids. *Appl. Energy* **2021**, 287, No. 116576.



- (34) Zhong, D. L.; Daraboina, N.; Englezos, P. Coal Mine Methane Gas Recovery by Hydrate Formation in a Fixed Bed of Silica Sand Particles. *Energy Fuels* **2013**, *27*, 4581–4588.
- (35) Zhong, D. L.; Lu, Y. Y.; Sun, D. J.; Zhao, W. L.; Li, Z. Performance Evaluation of Methane Separation from Coal Mine Gas by Gas Hydrate Formation in a Stirred Reactor and in a Fixed Bed of Silica Sand. *Fuel* **2015**, *143*, 586–594.
- (36) Zhong, D. L.; Ding, K.; Lu, Y. Y.; Yan, J.; Zhao, W. L. Methane Recovery from Coal Mine Gas Using Hydrate Formation in Water-in-Oil Emulsions. *Appl. Energy* **2016**, *162*, 1619–1626.
- (37) Wu, Q.; Zhang, Q.; Zhang, B. Influence of Super-Absorbent Polymer on the Growth Rate of Gas Hydrate. *Saf. Sci.* **2012**, *50*, 865–868.
- (38) Yan, J.; Lu, Y. Y.; Zhong, D. L.; Zou, Z. L.; Li, J. B. Enhanced Methane Recovery from Low-Concentration Coalbed Methane by Gas Hydrate Formation in Graphite Nanofluids. *Energy* **2019**, *180*, 728–736.
- (39) Rossi, F.; Filipponi, M.; Castellani, B. Investigation on a Novel Reactor for Gas Hydrate Production. *Appl. Energy* **2012**, *99*, 167–172.
- (40) Zhao, J.; Tian, Y.; Zhao, Y.; Cheng, W. Experimental Investigation of Effect on Hydrate Formation in Spray Reactor. *J. Chem.* **2015**, *2015*, No. 261473.
- (41) Cai, J.; Xu, C. G.; Xia, Z. M.; Chen, Z. Y.; Li, X. S. Hydrate-Based Methane Separation from Coal Mine Methane Gas Mixture by Bubbling Using the Scale-up Equipment. *Appl. Energy* **2017**, *204*, 1526–1534.
- (42) Cheng, C. X.; Tian, Y. J.; Wang, F.; Wu, X. H.; Zheng, J. L.; Zhang, J.; Li, L. W.; Yang, P. L. Experimental Study on the Morphology and Memory Effect of Methane Hydrate Reformation. *Energy Fuels* **2019**, *33*, 3439–3447.
- (43) Veluswamy, H. P.; Wong, A. J. H.; Babu, P.; Kumar, R.; Kulprathipanja, S.; Rangsunvigit, P.; Linga, P. Rapid Methane Hydrate Formation to Develop a Cost Effective Large Scale Energy Storage System. *Chem. Eng. J.* **2016**, *290*, 161–173.
- (44) Jiang, L.; Xu, N.; Liu, Q.; Cheng, Z.; Liu, Y.; Zhao, J. Review of Morphology Studies on Gas Hydrate Formation for Hydrate-Based Technology. *Cryst. Growth Des.* **2020**, *20*, 8148–8161.
- (45) Babu, P.; Linga, P.; Kumar, R.; Englezos, P. A Review of the Hydrate Based Gas Separation (HBGS) Process Forcarbon Dioxide Pre-Combustion Capture. *Energy* **2015**, *85*, 261–279.
- (46) Linga, P.; Kumar, R.; Lee, J. D.; Ripmeester, J.; Englezos, P. A New Apparatus to Enhance the Rate of Gas Hydrate Formation: Application to Capture of Carbon Dioxide. *Int. J. Greenhouse Gas Control* **2010**, *4*, 630–637.
- (47) Prasad, P. S. R.; Shiva Prasad, K.; Thakur, N. K. Laser Raman Spectroscopy of THF Clathrate Hydrate in the Temperature Range 90–300 K. *Spectrochim. Acta, Part A* **2007**, *68*, 1096–1100.
- (48) Prasad, P. S. R.; Sowjanya, Y.; Shiva Prasad, K. Micro-Raman Investigations of Mixed Gas Hydrates. *Vib. Spectrosc.* **2009**, *50*, 319–323.
- (49) Cai, J.; Tao, Y. Q.; von Solms, N.; Xu, C. G.; Chen, Z. Y.; Li, X. Sen. Experimental Studies on Hydrogen Hydrate with Tetrahydrofuran by Differential Scanning Calorimeter and In-Situ Raman. *Appl. Energy* **2019**, *243*, 1–9.
- (50) Florusse, L. J.; Peters, C. J.; Schoonman, J.; Hester, K. C.; Koh, C. A.; Dec, S. F.; Marsh, K. N.; Sloan, E. D. Stable Low-Pressure Hydrogen Clusters Stored in a Binary Clathrate Hydrate. *Science* **2004**, *306*, 469–471.
- (51) Lee, H.; Lee, J. W.; Kim, D. Y.; Park, J.; Seo, Y. T.; Zeng, H.; Moudrakovsk, I. L.; Ratcliffe, C. I.; Ripmeester, J. A. Tuning Clathrate Hydrates for Hydrogen Storage. *Nature* **2005**, *434*, 743–746.
- (52) Mao, W. L.; Mao, H. k.; Goncharov, A. F.; Struzhkin, V. V.; Guo, Q.; Hu, J.; Hu, J.; Hemley, R. J.; Somayazulu, M.; Zhao, Y. Hydrogen Clusters in Clathrate Hydrate. *Science* **2002**, *297*, 2247–2249.
- (53) Cai, J.; Zhang, Y.; Xu, C. G.; Xia, Z. M.; Chen, Z. Y.; Li, X. Sen. Raman Spectroscopic Studies on Carbon Dioxide Separation from Fuel Gas via Clathrate Hydrate in the Presence of Tetrahydrofuran. *Appl. Energy* **2018**, *214*, 92–102.
- (54) Studies on Temperature Characteristics and Initial Formation Interface during.Pdf.
- (55) Sum, A. K.; Burruss, R. C.; Sloan, E. D. Measurement of Clathrate Hydrates via Raman Spectroscopy. *J. Phys. Chem. B* **1997**, *101*, 7371–7377.
- (56) Tulk, C. A.; Klug, D. D.; Ripmeester, J. A. Raman Spectroscopic Studies of THF Clathrate Hydrate. *J. Phys. Chem. A* **1998**, *102*, 8734–8739.
- (57) Moryama, C. T.; Sugahara, T.; Yatabe Franco, D. Y.; Mimachi, H. In Situ Raman Spectroscopic Studies on Small-Cage Occupancy of Methane in the Simple Methane and Methane + Deuterated Tetrahydrofuran Mixed Hydrates. *J. Chem. Eng. Data* **2015**, *60*, 3581–3587.